Effects of surface roughness and mineralogy on the sorption of Cm(III) on crystalline rock

Demnitz, M.; Molodtsov, K.; Schymura, S.; Schierz, A.; Müller, K.; Jankovsky, F.; Havlova, V.; Stumpf, T.; Schmidt, M.;

Originally published:

August 2021

Journal of Hazardous Materials 423(2021)Part A, 127006

DOI: https://doi.org/10.1016/j.jhazmat.2021.127006

Perma-Link to Publication Repository of HZDR:

https://www.hzdr.de/publications/Publ-32811

Effects of surface roughness and mineralogy on the sorption of Cm(III) on crystalline rock

M. Demnitz,[a] K. Molodtsov,[a] S. Schymura,[b] A. Schierz,[a] K. Müller,[a] F. Jankovsky,[c] V. Havlova,[c] T. Stumpf,[a] M. Schmidt[a]*

[a)] *Helmholtz-Zentrum Dresden-Rossendorf e.V., Institute of Resource Ecology, Bautzner Landstraße 400, 01328 Dresden, Germany*

[b)] *Helmholtz-Zentrum Dresden-Rossendorf e.V., Institute of Resource Ecology, Research Site Leipzig, 04318 Leipzig, Germany*

[c)] *ÚJV Rez, a.s., Hlavni 130, Rez, 250 68 Husinec, Czech Republic*

*Corresponding author:

Moritz Schmidt
email : moritz.schmidt@hzdr.de
phone : +49 351 260 3156

keywords: curium; µTRLFS; crystalline rock; granite; sorption

Abstract:

Crystalline rock is one of the host rocks considered for a future deep geological repository for highly active radiotoxic nuclear waste. The safety assessment requires reliable information on the retention behavior of minor actinides. In this work, we applied various spatially resolved techniques to investigate the sorption of Curium onto crystalline rock (granite, gneiss) thin sections from Eibenstock, Germany and Bukov, Czech Republic. We combined Raman-microscopy, calibrated autoradiography and µTRLFS (*micro-focus time-resolved fluorescence spectroscopy*) with vertical scanning interferometry to study in situ the impact of mineralogy and surface roughness on Cm(III) uptake and molecular speciation on the surface. Heterogeneous sorption of Cm(III) on the surface depends primarily on the mineralogy. However, for the same mineral class sorption uptake and strength of Cm(III) increases with growing surface roughness around surface holes or grain boundaries. When competitive

sorption between multiple mineral phases occurs, surface roughness becomes the major retention parameter on low sorption uptake minerals. In high surface roughness areas primarily Cm(III) inner-sphere sorption complexation and surface incorporation are prominent and in select sites formation of stable Cm(III) ternary complexes is observed. Our molecular findings confirm that predictive radionuclide modelling should implement surface roughness as a key parameter in simulations.

Abbreviations:

EPMA:	electron probe micro analysis
ISS:	inner-sphere sorption
LI:	luminescence intensity
LSC:	liquid scintillation counting
OSS:	outer-sphere sorption
PXRD:	powder x-ray diffraction
ROI:	region of interest
SF:	surface
TRLFM:	time-resolved laser fluorescence microscopy
TRLFS:	time-resolved laser-induced fluorescence spectroscopy
URF:	Underground Research Facility
VSI:	vertical scanning interferometry
µTRLFS:	micro-focus time-resolved laser-induced fluorescence spectroscopy
µXRF:	micro x-ray fluorescence spectrometry

1. Introduction

The management of highly radioactive waste is one of the major technical and social challenges. Worldwide, underground disposal over the course of hundreds of thousands of years in deep geological repositories is considered to be the safest option for nuclear waste.[1-5] The radioactive waste containers will be surrounded by technical, geoengineered and geological barriers to fulfill safety functions in order to prevent migration of radionuclides towards the biosphere.[6-13] The assessment of safety performance of those barriers is therefore of utmost priority and will depend on reliable and complete thermodynamic data sets and a molecular level understanding of all relevant retention and mobilization mechanisms.

Besides salt and clay, crystalline rock is one of the preferred host rock environments considered in many countries, such as Germany or the Czech Republic, for the construction of a nuclear waste repository for high-level radioactive waste.[14-20] This is due to its strong geotechnical stability (and thus facile construction of the repository), low permeability, and low solubility. Crystalline rocks, such as granite, granodiorite, gneiss and other metamorphic rocks, usually consist of a wide set of minerals in varying amounts. However, the most abundant constituents, that are usually present, are quartz, feldspar, and mica. They are accompanied by varying amounts of accessory mineral phases e.g., pyrite, titanite, or prehnite.

Several previous studies focused on the sorption of different radionuclides on these individual phases, mainly in the form of mineral powders.[21-33] Using batch sorption experiments information on the retention capabilities of the minerals - ideally by retardation coefficients - with regard to the individual radionuclides were obtained. By combining batch sorption with spectroscopic, microscopic, and quantum chemical approaches details on the retention mechanisms on the molecular scale can be obtained. However, heterogeneous crystalline rocks surfaces are more complex than those of homogeneous mineral powders. On complex multi-mineral surfaces radionuclide sorption behavior is influenced by co-dependencies between mineral phases and heterogeneous surface topographies, especially around mineral grain boundaries.[34-38] Hence, the need arises for an analytical tool capable of deriving molecular level information with sub-mineral grain spatial resolution to visualize and explain inter- and intra-mineral heterogeneities in radionuclide sorption.

The highest radiotoxicity in spent nuclear waste, once the short-lived fission products have decayed after ~300 years, can be attributed to the transuranium elements Np, Pu, Am, and Cm.[39, 40] Of these, Am and Cm will be present in their trivalent state. Moreover, Pu maybe also at least partially present as Pu(III) due to the reducing environment encountered in deep

geological repositories.[41-45] The actinides Cm, Am, and Pu in their trivalent form exhibit very similar chemical behavior.[46, 47] In this work, we use Cm(III) as a representative of the actinide group mentioned above, which can be used as a molecular probe, because of its excellent luminescence properties. This allows the measurement of Cm(III) concentrations down to approximately ~10^{-12} M, that can be considered close to reality in the context of actinide concentrations in a nuclear waste repository.[48]

Spectroscopic description of actinide surface sorption

Time-resolved laser-induced fluorescence spectroscopy (*TRLFS*) is a convenient method to study the speciation of Cm(III) in aqueous solution and at solid/water interfaces by monitoring its luminescence peaks shifts. Cm(III) emission bands will be bathochromically shifted ("red shift") when the first coordination shell of the emitting Cm(III) ion changes. The Cm(III) aquo ion luminesces at 593.8 nm,[49] when water molecules in its first hydration shell are substituted by chemical bonds to a mineral surfaces the luminescence signal will be red-shifted (λ_{max} > 593.8 nm).[50] The more water molecules are replaced by stronger ligands from the surface or solution, e.g. in the formation of surface incorporation species or ternary surface complexes, the stronger is the observed red-shift. [21, 51] In contrast, Cm(III) bound to the surface with its hydration shell intact will luminesce at the same λ_{max} = 593.8 nm as the aquo ion, as its first coordination shell has not changed. [22] Thus, the peak positions of Cm(III) luminescence can be used to distinguish inner-sphere sorption (ISS) complexes, chemically bound to the surface from electrostatically bound, fully hydrated outer-sphere sorption (OSS) complexes (see Figure 1).

Additional structural information can be obtained from the time dependent decay of the luminescence. Quenching processes will shorten the luminescence lifetime by providing a non-luminescent pathway for bridging the energy gap between excited and ground state. In the scope of our experiments the most relevant quencher is water, which quenches Cm(III) luminescence by OH-vibrations. Therefore the more water molecules surround the Cm(III) the higher the quenching effect and in turn the shorter the luminescence lifetime. Cm(III) is typically coordinated by nine water molecules in its first coordination sphere, which corresponds to a lifetime of 68 µs.[50] In contrast, complexation of Cm(III) with other ligands (or a mineral surface) that replace water molecules usually leads to longer lifetimes. This correlation is influenced by the presence of other quenching pathways, such as energy transfer to transition metals, e.g., iron, whose presence must be considered when interpreting lifetime data. This means a lifetime analysis can give us structural insight and information about the complexation

strengths of Cm(III) and formed species: OSS, weak/strong ISS, surface incorporation, ternary complexes and total incorporation (see Figure 1). The combination of luminescence spectrum and lifetime analysis is a well-established method to describe Cm(III) speciation in water and at mineral-water interfaces.[23, 26, 32, 46, 48, 50, 52-55]

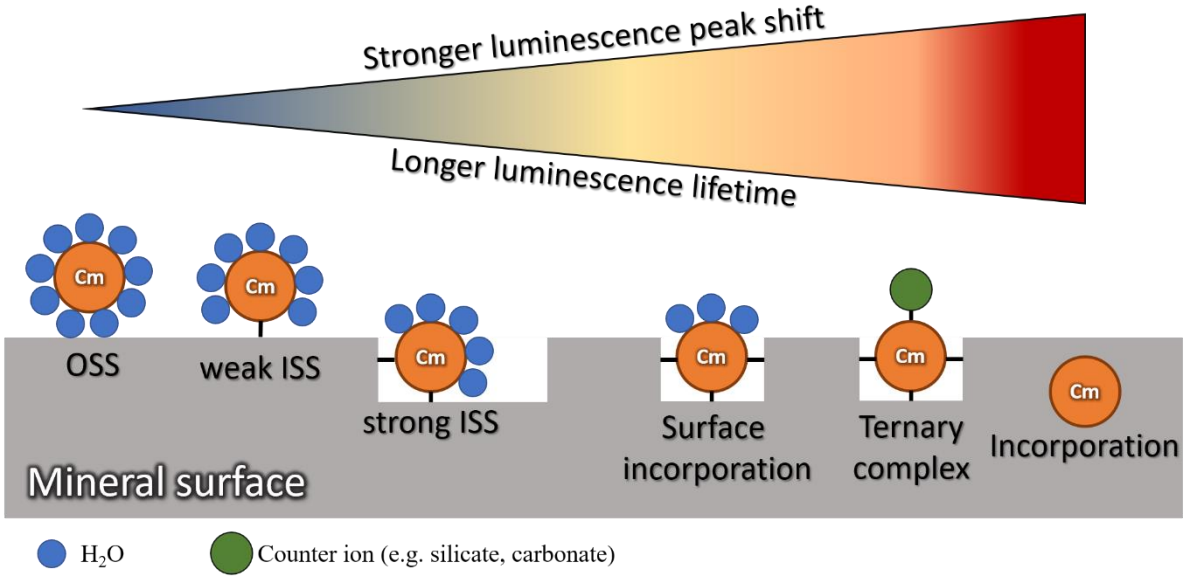

Figure 1: Simplified scheme for Cm(III) sorption on a mineral surface and the thereby formed complexes. OSS = outer-sphere sorption; ISS = inner-sphere sorption. Cm(III) species with 9 surrounding water molecules are assigned to be OSS complexes. Complexes with 7 – 8 / 5 – 6 water molecules are weak/strong ISS species respectively. Cm(III) with only 1 – 4 water molecules remaining in the first coordination sphere are counted as surface (SF) incorporation species, while no water corresponds to ternary complexes with carbonate/silicate or complete mineral bulk incorporation.

Sorption of trivalent lanthanides and actinides has been studied on individual constituents of crystalline rock, such as quartz, feldspar, and mica. On quartz sorption of Cm(III) was investigated using TRLFS in the pH range of 3.8 to 9.5.[50] Starting at pH 4, Cm(III) sorbs onto the quartz surface as an ISS complex, which then hydrolyzes starting at a pH of 5.5. Luminescence peak maxima were located at 601.4 and 603.6 nm, with both complexes sharing a common luminescence lifetime of 123 ± 10 µs, which corresponds to five coordinating water molecules (or OH^- ligands) within their hydration shell. In a recent study sorption of Ln(III)/Am(III)/Cm(III) on K-feldspar was investigated using batch sorption experiments and TRLFS.[21] Sorption edge studies ($[M^{3+}] = 5.2 \cdot 10^{-8}$ M – 10^{-4} M) showed that below pH 5 only small amounts of trivalent metals sorb on K-feldspar in the form of OSS complexes. Above pH 5 sorption uptake quickly increases up to pH 7.8 where complete sorption was achieved. Using TRLFS a total of five different sorbed Cm(III) species were identified: OSS below pH 4.4, three ISS complexes of varying strength above pH 4.4, and a ternary surface complex presumably involving silicate at pH exceeding 10.0.

To the best of our knowledge no studies of Cm(III) sorption on heterogeneous crystalline rocks are currently available in the literature. However, a few studies on the sorption of trivalent lanthanides on heterogeneous crystalline rocks have been published. Eu(III) is usually used as a chemical analogue for trivalent actinides. Eu(III) sorption ([Eu] = 1 µM) on granite was quantified in the presence and absence of carbonate.[56] It was shown that the sorption process is independent of carbonate, with Eu(III) sorption starting at pH 3, slowly increasing to around 20% at pH 5 from where a steep increase to 100% sorption up to pH 8 was observed. Time-resolved laser fluorescence microscopy (*TRLFM*) was used to study Eu(III) sorption on a granite surface consisting mainly of biotite, plagioclase, K-feldspar, and quartz.[57] Using the spatially-resolved technique it was found that Eu(III) sorbs heterogeneously on the surface. Ishida et al. (2009) proposed that sorption is governed by the feldspar phases, with only little sorption on quartz and biotite, while sorption on all three mineral phases occurs primarily around surface cracks. It was concluded that surface roughness has a major effect on the sorption process.[57]

Using micro-focus time-resolved laser-induced fluorescence spectroscopy (*µTRLFS*), electron probe micro analysis (*EPMA*), micro X-ray fluorescence spectrometry (µXRF) and autoradiography the sorption of Eu(III) on a granite thin section composed of feldspar, quartz and biotite at pH 8.0 was recently investigated by our group.[38] With autoradiography the sorption uptake on a thin section was assessed showing that sorption on quartz is low with comparatively high sorption uptake on biotite and feldspar mineral grains. µTRLFS confirmed the heterogeneous inter-mineral differences in sorption of Eu(III) on the granite surface. Luminescence intensity of Eu(III) was detected in decreasing amounts on feldspar, quartz and biotite in that order. Biotite as a Fe-bearing mineral was found to quench the luminescence of the Eu(III), explaining the deviation from the autoradiography signal that showed sorption amounts similar to feldspar. Additionally, the µTRLFS provided sufficient spatial resolution to identify increased sorption uptake in the mineral grain boundary region between feldspar and biotite. Also, on the quartz surface heterogeneous sorption was observed. Sorption is limited to only a few places but binding is strong, indicating sorption to surface sites with limited availability, most likely surface defect sites.[38]

We performed a similar Eu(III) sorption study on a gneiss thin section sample at pH 7.5.[58] The gneiss has a more complex mineralogy. It mainly consisted of quartz, feldspar, and amphibole, but contained a large number of minor mineral phases. Autoradiography showed that sorption uptake is highest on chlorite, intermediate on amphibole, and lowest on feldspar and quartz. Chlorite could not be analyzed by µTRLFS due to its high Fe content, thus µTRLFS

found the highest amount of Eu(III) sorbed on the minor mineral phase prehnite, while less sorption occurred on feldspar and no signal could be detected on quartz. Surprisingly, the two materials - granite and gneiss - show clearly deviating behavior, despite consisting of the same main constituents. The high sorption uptake on amphibole and prehnite, limits the amount of Eu(III) available for sorption on feldspar and especially quartz. The same process also affects the speciation of Eu(III) at the interface, resulting in the preferential formation of stronger bound Eu(III) surface species on feldspar.

Our two prior studies demonstrate that surface topography can lead to variations in the retention behavior. This is most prominent in the case of mineral grain boundaries but also intra-mineral roughness variation that is reflecting different availability of, e.g., kink or defect sites, which can lead to significant sorption heterogeneities. In the previous studies, the topography of the surface was, however, not known, but had to be inferred from differences in Eu(III)'s sorption behavior. In this study we expand the investigation of the sorption behavior of Cm(III) on the same granite and gneiss used in our earlier Eu(III) investigations using Raman-microscopy, autoradiography, and µTRLFS in combination with vertical scanning interferometry (VSI). Vertical scanning interferometry allows the determination of the surface topography with a vertical spatial resolution in the nanometer range. From this data we derive surface roughness in the form of the S_q parameter, the root mean square deviation of the height data that serves as a suitable proxy for sorption site variations. The mineral phases present on the surface are identified by Raman-microscopy. Sorption uptake of Cm(III) can be determined by autoradiography and partially µTRLFS, allowing us to compare both methods with each other. Most importantly, µTRLFS allows us to obtain spatially-resolved Cm(III) speciation information on the molecular level from luminescence spectra and luminescence lifetimes. Because there is no natural Cm background in the mineral phases, data interpretation is expected to be easier than in the case of Eu(III), which is often naturally incorporated in minerals. Furthermore, Cm(III) possesses a higher luminescence yield, which permits use of lower concentrations of Cm(III) at 1 µM in comparison to Eu(III).

This sophisticated combination of techniques allows us to correlate uptake and speciation of Cm(III) on natural rock surfaces with the underlying surface topography at close to realistic conditions.

2. Materials and methods

2.1 Sample preparation

The Eibenstock granite sample was obtained from a former uranium mine in Eibenstock, Germany. The material has been used in a previous Eu(III) sorption study applying µTRLFS. As described elsewhere the granite mainly consists of quartz, K-feldspar, biotite, and muscovite.[38] In order to be used in batch-sorption experiments with powdered rock samples the specimen were cut down using a Buehler AbrasiMatic 300 abrasive cutter and a Buehler IsoMET low speed saw, ground down using an agate-based Fritsch pulverisette 2 mortar grinder and perpetually sieved using a Retch Vibro sieving setup to obtain grain sizes below 63 µm. Parts of the rock were cut into 28×23 mm slabs, which were embedded in epoxy resin. They were polished down to a thickness of 200 µm, followed by a fine polishing using two sizes of diamond crystals (3 and 1 µm), and finally a chemical silica suspension. Before the sorption experiment, the sample was washed with deionized water (MilliQ, 18.2 MΩ·cm) and ethanol (95%) followed by 15 min of ultrasonification in deionized water in an ultrasonic bath; subsequently it was washed with deionized water and ethanol again.

The Bukov gneiss sample was part of a drill core obtained from the Underground Research Facility Bukov (Bukov URF), Czech Republic and consists mainly of feldspar, amphibole, mica and quartz, as previously described.[58] Powder and thin section samples were produced in the same manner as for the Eibenstock granite.

In order to perform sorption edge studies 2 g/L of crystalline rock powder were suspended in MilliQ water. NaCl (Carl Roth GmbH & Co. KG; >99.5%) was used as a background electrolyte to achieve an ionic strength of 0.1 M. The pH of the samples was adjusted to pH = 0.5 – 9.1 using HCl (Carl Roth GmbH & Co. KG; 37%) and NaOH (Carl Roth GmbH & Co. KG; 99%) before adding $5 \cdot 10^{-7}$ M of ^{248}Cm(III) or [^{152}Eu]Eu(III). The samples were shaken over several days until an equilibrium condition was reached. For the analysis of Cm(III) and Eu(III) remaining in solution, the samples were centrifuged (4020 × g) and subsequently a 100 µL aliquot of the supernatant of each sample was added into 10 mL Ultima Gold™ for liquid scintillation counting (*LSC*; HIDEX 300 SL). Afterwards the final pH of the sample was measured. See SI for more details.

For Cm(III) sorption experiments on the thin sections a solution containing 10^{-6} M Cm(III) at pH 8.0 and I = 0.1 M NaCl was prepared. The low Cm(III) concentration ensures that no precipitation of Cm(III) on the surface due to hydrolysis takes place.[21] The thin section was

then placed upside down into the sorption solution in a custom-made sorption cell (see Figure S13 in the SI). The cell was sealed and shaken at least 7 days until equilibrium was reached. The thin section was taken out and washed (pH = 8.0; I = 0.1 M NaCl) to remove excess non-sorbed Cm(III).

2.2 Powder X-ray Diffraction

Powder X-ray diffraction (*PXRD*) was used to qualitatively determine the bulk mineralogy of both samples. Diffractograms of ground powder samples were measured using a Rigaku MiniFlex 600 with Cu Kα (λ = 1.54184 Å) as its X-ray source. The energy was set to 600 W while measuring in a continuous scan mode. The Rigaku D/teX Ultra Si strip-one dimensional detector was used. The 2θ region between 5.0° and 60.0° was measured with a 0.05° resolution. The determined mineral compositions are averages and the percentages of the composition may vary within the crystalline rock.

The quantitative bulk mineral composition of Eibenstock granite was determined using PXRD and reported elsewhere.[38] It consists mainly of quartz (45 wt%), feldspar (42.5 wt%), and mica (11.5 wt%).

The quantitative Bukov gneiss bulk mineral composition was determined by PXRD as well and reported elsewhere.[58] It consists mainly of feldspar (45.5 wt%), amphibole (30.3 wt%), quartz (13.5 wt%), mica (9.2 wt%), and biotite (1.5 wt%).

2.3 Optical microscopy

Transmitted light microscopy images of the entire thin sections were taken using a Leica DM-EP equipped with a Jenoptik Progres Gryphax camera. Additionally, reflected light microscopy images of the regions of interest (ROIs) were photographed using a LabRam Aramis (Horiba) Raman-microscope with a 10× magnification objective.

2.4 Raman-microscopy

Several regions of interest (ROIs) were chosen via microscopic survey of each thin section sample based on the presence of interesting features such as presumed mineralogy and surface roughness (see Figure 2 a). To determine surface mineralogy the ROIs were measured using a LabRam Aramis (Horiba) Raman-microscope. A 532 nm continuous wave laser at 50 mW was used and the slit and pin-hole diameter were set to 200 and 300 µm, respectively. For each ROI, at least a 1×1 mm² area was measured using a grid of 15 to 20 µm. The obtained data was

treated using a Python-based software developed in-house (pycroTRLFS EVAL, HZDR, Germany) to obtain relevant peak positions, which were then compared to reference mineral spectra from the RRUFF database (see SI Figure S12).[38, 59]

2.5 Vertical scanning interferometry

Vertical scanning interferometry measurements to determine surface topography were carried out using a Sensofar s neox interferometer with three different Nikon Interferometry objectives DI20x, DI50x and DI100x (see SI Table S1 for specifications and achieved resolutions). The interferometer was run using the white light interferometry mode and the data was evaluated using the SensoMap Premium 7.4 (DigitalSurf). Surface height data with a resolution of 1 nm in z-direction is produced by the software from the interference of the light reflected by the sample surface with a reference beam. Depending on the different optical pathways set by the surface height an interference signal is obtained for every pixel from which the surface height can be derived at the point of maximum modulation of the interference pattern.[60] The surface roughness was characterized using the surface parameter S_q, the root mean square of the height difference. To generate surface roughness maps S_q was calculated for every pixel using a 7×7 pixel sliding window.

2.6 Autoradiography

Autoradiography was used to determine the quantitative sorption uptake of Cm(III) on the thin sections. Absolute concentration values were obtained by calibrating the autoradiography image using activity standards of known Cm(III) concentrations that were exposed to the imaging plate in parallel to the thin section samples. To produce the activity standards droplets of 1 µL of acidic (HCl) solutions containing between 0.2 – 5 µM of Cm(III) with two replicates for each concentration step were pipetted on a glass slide. Using the calibration function of ImageJ the grey value of the autoradiography image was transformed into concentration data, with the integrated density being equal to the amount of substance in pmol and the mean value denoting the concentration in pmol/cm^2 of the projected area (see Figures S10/S11 in SI for autoradiography image calibration).

The Cm-loaded thin section was placed on a Storage Phosphor Screen BAS-IP SR 0813 E Super Resolution autoradiography plate separated by a 2.5 µm thick plastic foil to avoid contamination of the autoradiography plate. This setup was pressed tightly together by two plastic plates using screws and kept for one week within a light-proof box. After 7 days of exposure time the plate was read out using an Amersham Typhoon Biomolecular Imager (GE

Lifesciences) with a pixel size of 10 µm. Note that this is not equal to the physical resolution of the activity distribution, which is lower due to the isotropic emission and scattering of the alpha radiation, which was additionally shielded by the thin plastic foil.[58]

2.7 µTRLFS

By applying µTRLFS we are able to gain semi-quantitative information on the Cm(III) sorption uptake and qualitative information on its speciation on the surface. From the luminescence lifetime we can calculate the number of water molecules surrounding Cm(III) and gain insight in its coordination environment from the red shift in the measured spectra. This allows us to use Cm(III) as a probe to determine molecular binding motives.

The µTRLFS setup we used has been described previously.[38] The laser pulse energy was set to 20 to 25 µJ. To avoid laser ablation of the surface, the sample was moved out of the laser's focal plane by moving the z-axis of the sample stage 60 µm. This resulted in a laser spot size of around 20 µm. Each 1×1 mm^2 ROI was scanned using a 20 µm grid resulting in 2601 luminescence spectra per ROI.

The luminescence spectra were evaluated using a Python based software (pycroTRLFS EVAL, HZDR, Germany).[38] Each pixel corresponds to a full luminescence spectrum. An appropriate range for peak integration was chosen, from which a linear background was subtracted, and the intensity was integrated to obtain the total luminescence intensity. The peaks were fit using a Gaussian function to yield the peak maxima, which is used to assess the red shift that is associated with the strength of the complexation as detailed above.

Luminescence lifetimes were measured on selected pixels. The fitting of the lifetimes was performed by using mono-, bi-, and triexponential decay functions. An appropriate fit was chosen based on a determination coefficient close(r) to a value of one, while keeping the error range of the lifetimes small. From the lifetimes it is possible to calculate the number of water molecules in Cm(III)'s first coordination sphere using Kimura's equation:[61]

$$n(H_2O) = \frac{0.65\ \text{ms}}{\tau} - 0.88 \quad (1)$$

As no more solution is present during our measurements the samples surface can be considered dry. Therefore, we will interpret species with fully hydrated Cm(III) as OSS complexes, since free Cm(III) aquo ions are only present in solution. Any change in peak position and luminescence lifetime then indicates substitution of water in the first coordination sphere by

other ligands. For our experiments these will predominantly stem from the surface and the species can thus be identified as ISS complexes, or even more strongly bound surface species (see section 3.1 and 3.2).

3. Results

3.1 Sorption of Cm(III) on Eibenstock granite

Mineralogy of the Eibenstock granite

Optically the Eibenstock thin section consists of three differently colored mineral grain types (see Figure 2 a), which size ranges from hundreds of µm to a few mm. According to the PXRD results (see section 2.2) we could identify the grains as quartz (white), feldspar (black), and mica (brown) as seen in optical microscopy.

For a more precise identification of the mineral phases four different regions of interest (ROIs) were investigated using Raman-microscopy (see orange rectangles in Figure 2 a). From the Raman spectra, it was concluded that feldspar and quartz were present on all regions. The mica composition could not be determined conclusively, but the spectra suggest mica is mostly present as muscovite. Topaz, a nesosilicate mineral, was also identified in ROI 2. In Figure 4 a ROI 1 is shown exemplarily. It primarily consists of feldspar, quartz, and mica. Details of the other ROIs are given in the SI (see Figures S3-S5)

Surface topography

Vertical scanning interferometry (see Figure 2 b, Figure 4 b and Figures S3-S5) revealed distinct topographical surface features for all minerals. Mica surfaces are characterized by elongated cracks and streaks up to several micrometers deep. Feldspar grains feature a multitude of surface pits of about 200 nm depth. Cracks similar in depth to what was seen on mica are found on topaz, however, covering a much larger area than for mica. Quartz surfaces are characterized partially by surface pits of about 200 nm depth. A quantification of these different features by proxy using the surface roughness parameter S_q allows us to rank the minerals according to their average S_q value with the according root mean square error: surface roughness is the highest on topaz with an S_q value of 503 ± 45 nm, followed by mica with 111 ± 11 nm and feldspar with 95 ± 6 nm. Quartz showed the lowest S_q value of 75 ± 15 nm. These averaged values correlate with the occurrence and depth of pits and cracks on the different minerals and are the result of significant intra-mineral heterogeneities as they are composed of the very rough pit and crack edges and rather smooth areas in between, or areas with high pit/crack densities and smooth areas without these structural features. While the surface topography of the thin section cannot be taken directly as an analogue for naturally occurring fissure topography, surface sites occurring on topography features of the thin section

should also exist in nature. There the surface site concentration might differ, but the thin section allows us to control and semi-quantitatively analyze the sites via surface roughness parameters.

In general, the most prominent topographical features besides the mineral textures mentioned above are the grain boundaries. The different resistances of the minerals to the thin section preparation procedures (sawing, polishing, etc.) result in height differences that create distinct features where different mineral grains meet. We find height differences of up to 400 nm between feldspar and quartz and up to 110 nm between feldspar and mica. The quartz/mica grain boundary height difference can reach up to 565 nm. Topaz difference in height to quartz is 175 nm and smaller than the topaz feldspar difference with 416 nm. Again, these height differences as well as the steepness of the grain boundary can be semi-quantitatively characterized using the S_q value. Doing so yields S_q values of up to 80 ± 3 nm for the feldspar/quartz boundary, 15 ± 2 nm for the feldspar/mica boundary, 190 ± 3 nm for the quartz/mica boundary and 108 ± 4 nm and 80 ± 2 nm for the topaz/quartz and topaz/feldspar boundaries, respectively.

Sorption uptake of Cm(III)

Firstly, sorption was quantified on bulk powder material as a function of pH using Cm(III) for Eibenstock granite. The relative uptake as a function of solution pH can be seen in Figure S1 in the SI: (a) Up to pH 3 no metal uptake from the solution can be observed, (b) from pH 3 to 5.2 sorption increases to around 30%. (c) Increasing the pH to 7.5 results in almost complete sorption of Cm(III). (d) Further increasing the pH from 7.5 onward resulted in no changes in sorption uptake. This sorption behavior is typical for trivalent metals on different mineral phases.[24, 27, 31, 62, 63] However, sorption on bulk material does not deliver information on the mechanism of Cm(III) sorption on the mineral surface and no differentiation between individual mineral phases is possible, which is why a spatially-resolved surface investigation of heterogeneous crystalline rock is required. From the sorption edge studies we determined the ideal pH for Cm(III) sorption experiments on the thin-sections to be pH 8.0, since here complete sorption takes place, but bulk precipitation should still be negligible.

To locally quantify the Cm(III) sorption uptake on Eibenstock granite (i.e. specific to each mineral phase) we used calibrated autoradiography as shown in Figure 2 c. Cm(III) sorption uptake on Eibenstock granite is quite heterogeneous. When considering each mineral phase separately, uptake decreases as follows: biotite > feldspar ~ topaz > quartz. Similar tendencies are seen for reported log K values in literature for Eu(III), which are directly comparable via the chosen reaction scheme (see SI Table S2). [64, 65] Our autoradiography analysis shows that

sorption occurs mainly on feldspar and biotite mineral grains showing over 300 pmol/cm^2 sorption uptake, while generally the sorption on quartz mineral grains is below 80 pmol/cm^2. Only in quartz areas with a higher inherent surface roughness the sorption uptake increases to a similar amount as observed on feldspar and mica (see black ellipses in Figure 2 b, c and Figures S2 – S5). The lower left part of the thin section shows high sorption uptake, which can be traced back to part of the thin section breaking in that area. This had no impact on the following measurements of ROI 1 – 4 but can be considered an artifact. The Cm(III) sorption uptake has now been quantified on each mineral phase, yet the molecular speciation of the sorbed Cm(III) has remained unknown, which is why we applied µTRLFS.

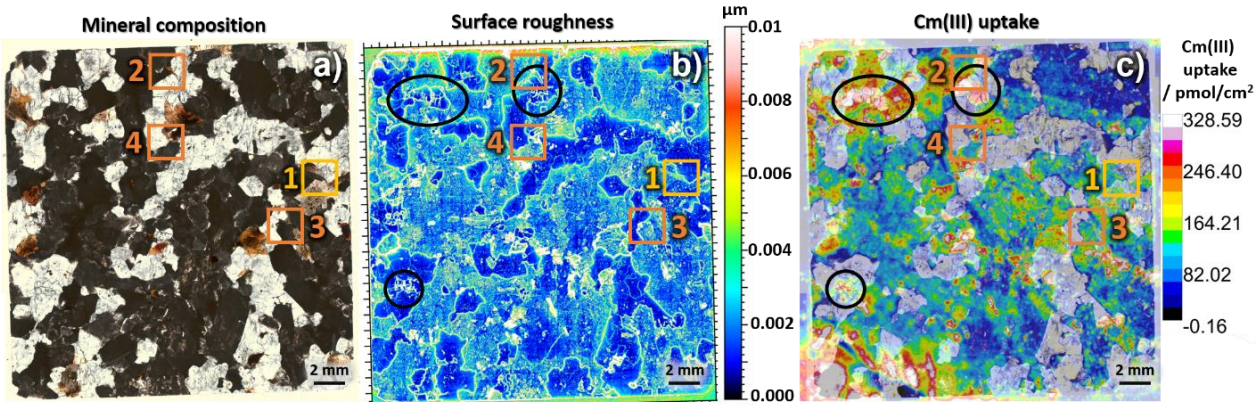

Figure 2: a) Optical image of the Eibenstock granite thin section with orange marked ROIs (for detailed ROI analysis see Figure 4 and Figure S3 – S5), b) surface roughness determined using interferometry (VSI) and c) Cm(III) sorption uptake determined using quantitative autoradiography. The black ellipses indicate high surface roughness/sorption uptake areas on quartz.

Using µTRLFS we can determine Cm(III) sorption uptake based on the integral luminescence intensity (LI) (see Figure 3 and for integration ranges see Figure *4*). More importantly, we can use the measured spectra to characterize Cm(III)'s bond strength to the surface from the observed red shift in comparison to the Cm(III) aquo ion and the number of water molecules remaining in its first coordination sphere from the measured lifetimes. On all ROIs (see Figure 3 and Figure S3-S5) we found that the overall distribution of the LI is heterogeneous not only between the different mineral phases, but also within the same mineral grains. LIs were found to be highest on feldspar and topaz, intermediate on quartz and only weak signals were detected on muscovite and other mica (LI ~ 25 : 3 : 1). In contrast, autoradiography showed high sorption uptake on mica. Most likely luminescence quenching takes place here, due to the high Fe content, hindering luminescence detection.

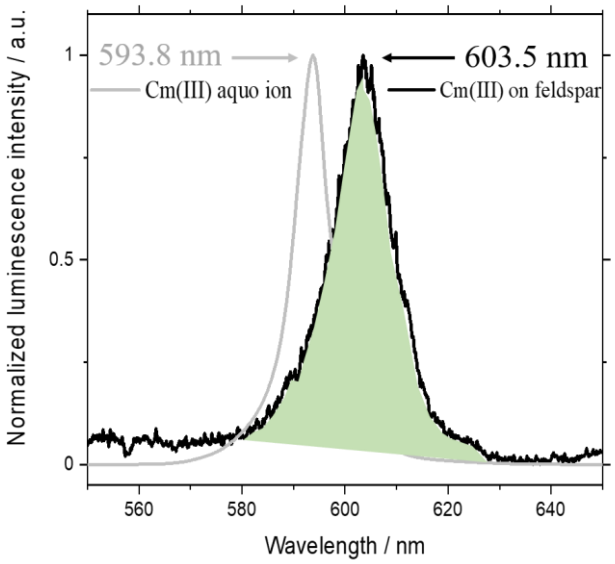

422

423 Figure 3: Exemplary high LI spectrum of Cm(III) sorbed on feldspar (black) and a non-complexed Cm(III) aquo ion in
424 solution (grey). The peak maxima are indicated by the arrows and the integral luminescence intensity by the green area. The
425 Cm(III) feldspar spectrum represents one pixel in the measured µTRLFS maps.

426 Speciation of Cm(III)

427 In the following section and in Figure 4 the focus is set on Cm(III)'s distribution and speciation
428 in ROI 1 (see Figure 2). Nevertheless, the results of the other ROIs (see SI Figures S3-S5) are
429 included in the discussion.

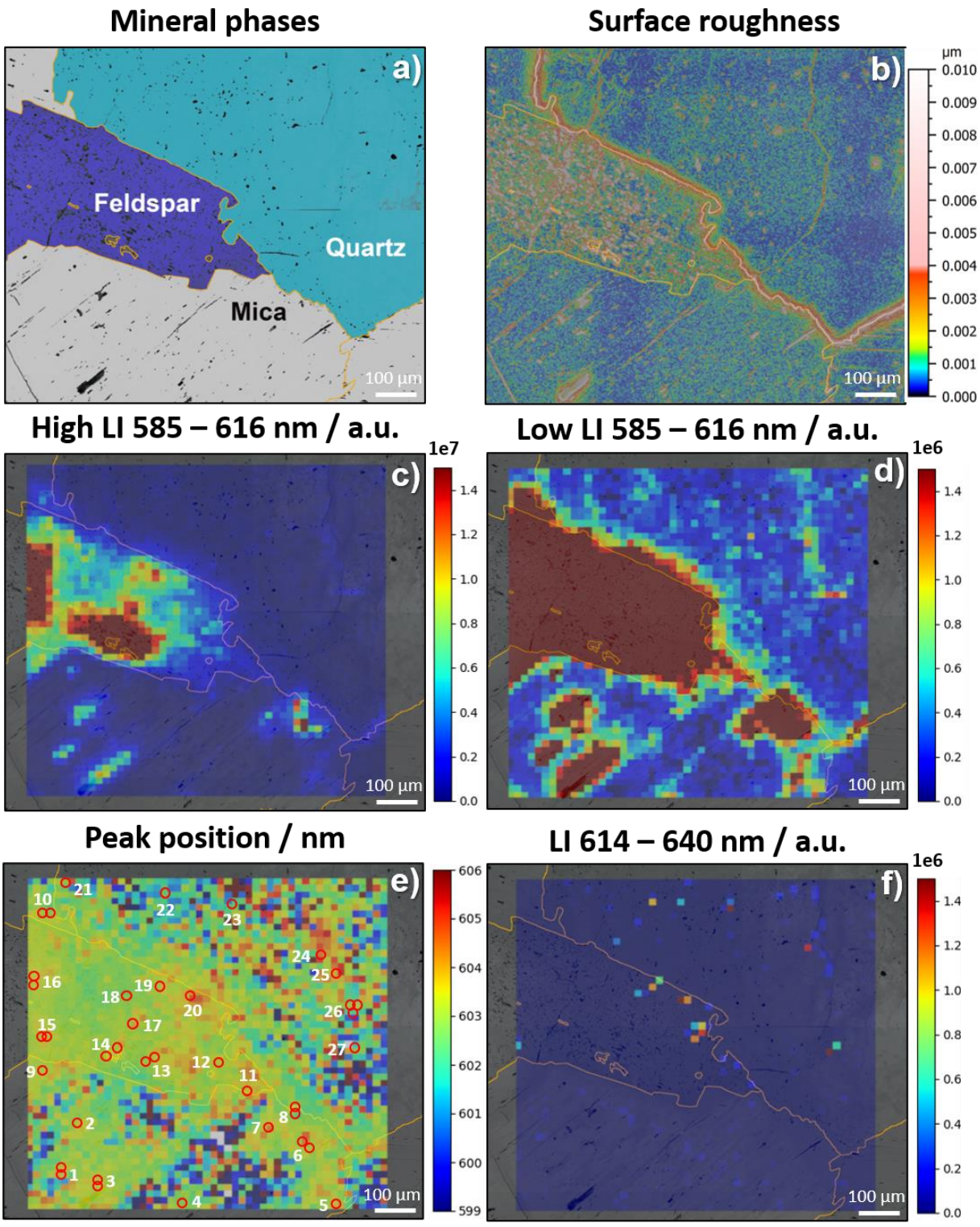

Figure 4: Analysis of ROI 1 on Cm(III) loaded Eibenstock granite: a) mineral composition (Raman-microscopy), b) surface roughness (S_q; interferometry), c) high luminescence regime of Cm(III) (µTRLFS; integral area) and d) the by a factor of 10 decreased scale of the low luminescence regime of Cm(III) (µTRLFS; integral area), e) by Gaussian peak fitting obtained peak maxima of the Cm(III) peaks (µTRLFS; lifetimes measurements spots indicated by red circles) and f) luminescence intensity of Cm(III) at higher wavelengths (µTRLFS; integral area).

ROI 1 is characterized by feldspar, quartz and mica mineral grains (see Figure 4 a). High surface roughness areas can be observed around feldspar surface pits, mica cracks, and the mineral grain boundaries of quartz with both, mica and feldspar (see Figure 4 b).

Within ROI 1 we observe that Cm(III) sorption occurs heterogeneously, with the sorption being highest on feldspar, especially in areas with a high surface roughness such as surface pits (compare Figure 4 b and c). When looking at the full range of LIs (see Figure 4 c) all other minerals appear homogeneous and show almost no sorption. A change in scales (see Figure 4 d) reveals that the distribution of Cm(III) is quite heterogeneous also on the other mineral phases, with distinct areas of higher sorption uptake.

Gaussian fitting of all Cm(III) luminescence spectra yields a map of the peak maximum in each pixel, which depends on the strength of the ligand field around Cm(III) and thus gives an indication of the bond strength to the surface (Figure 4 e).

Peak maxima on feldspar are located between 602 and 605 nm, indicating that ISS complexes of varying strength have formed. An additional strongly red-shifted Cm(III) peak can be detected at selected spots on feldspar, which also occurs on quartz and their grain boundary with each other (see Figure 4 f). On feldspar and the grain boundaries of feldspar and quartz this peak maximum is located between 621 and 625 nm. Cm(III) signals at wavelengths that clearly exceed 620 nm are typically incorporated species, red shifts of ternary complexes on a mineral surface are similar but typically less pronounced.[23, 66-70] Structural incorporation, however, appears unlikely, since the experiment time of just one week seems too low for Cm(III) incorporation into feldspar to take place.[71]

On quartz, sorption heterogeneity is only revealed when reducing the luminescence intensity scale by a factor of ten (Figure 4 d). In general, low levels of sorption are observed on quartz, occurring mainly in areas with increased surface roughness, especially at quartz' grain boundary with mica. Some low roughness areas on quartz had such a low LI that no peak fitting was possible. In areas with higher LI we observed peak maxima between 602 and 605 nm, showing the formation of ISS complexes with varying bond strength similar to feldspar. We also observed strongly red-shifted peaks at 625 – 630 nm on quartz, even more strongly shifted than similar features on feldspar, which would again indicate incorporation or ternary complex formation (see Figure 4 f). Such strong luminescence shifts exceeding 620 nm as we observe here on feldspar and quartz are typically associated with Cm(III) structurally incorporated into crystalline materials.[23, 66, 67, 70] However, our experimental procedure, in particular the short reaction time of only 7 d makes it appear unlikely that such a process could have occurred. The only other species which exhibit similar, albeit typically lower peak shifts (~610+ nm) are ternary surface complexes, which could here have formed by partial dissolution of a mineral to provide e.g. SiO_4^{4-} as a co-ligand. It remains unclear, why the ternary complexes would exhibit

such extraordinarily large red shifts, or how an incorporation process could occur in such a short time and our data do not allow an unambiguous identification. A possible explanation is the formation of a ternary complex from a SF incorporation species with an already high coordination number from the surface (see Figure *1*) in which the ligand from solution completes the coordination shell. Of course, such a species could also be considered as an incorporation species.

Generally, the LI on mica outside of areas with a high surface roughness - such as the surface cracks - is low, due to Fe quenching the luminescence[72] since high sorption uptake was seen in autoradiographic measurements. Peak maxima on mica range from 603 to 604 nm, indicating a more homogeneous distribution of ISS complexes.

On topaz found on ROI 2 (see Figure S3) we obtained high intensity signals close to mineral boundaries and cracks with peak maxima ranging from 599 to 601 nm, suggesting weaker ISS. In contrast smoother regions show comparatively lower LI, but stronger ISS with peak maxima of 601 up to 604 nm.

Luminescence lifetime measurements allow the determination of the detailed speciation of Cm(III) sorbed to the mineral surface by calculating the number of water molecules in the coordination sphere of the Cm(III). In summary, 137 individual lifetime measurements (see Table S3) were performed for all ROIs at different points as indicated by circles in Figure 4 e for ROI 1 and Figure S3 – S5 for ROIs 2 – 4. The points were chosen and evaluated depending on their surface roughness (smooth/rough) and proximity to mineral grain boundaries. In order to obtain a better differentiation between the formed species we categorized them: Cm(III) species with 9 surrounding water molecules are assigned to be OSS complexes. Complexes with 7 – 8 and 5 – 6 water molecules are weak and strong ISS species, respectively. Cm(III) with only 1 – 4 water molecules remaining in the first coordination sphere are identified as surface (SF) incorporation species, while no water corresponds to ternary complex formation with carbonate/silicate or complete mineral bulk incorporation. For a visual representation the reader is referred to Figure 1. The results of these measurements are listed in Table 1 sorted according to their mineral phases and surface roughness.

Table 1: Summary of measured lifetimes on all regions of interest on Eibenstock granite corresponding to mineral form and its topography features (ISS = inner-sphere sorption, OSS = outer-sphere sorption, SF = surface). For details the reader is referred to section 3.1. The error 0.5 for calculated water molecules originates from the (1) Kimura equation if only few data points or data points of the exact same value exist. For data sets with multiple data points the error was calculated by applying simple standard deviation. Smooth and rough surfaces were determined by visual inspection of the S_q distribution maps.

Mineral form	**n(H_2O)**	**Species**
Feldspar (smooth)	7.4 ± 0.5	Weak ISS (23%)

	5.7 ± 0.5	Strong ISS (47%)
	3.3 ± 0.7	SF incorporation (30%)
Feldspar (rough)	9.0 ± 0.5	OSS (5%)
	7.5 ± 0.5	Weak ISS (6%)
	5.1 ± 0.3	Strong ISS (26%)
	3.4 ± 0.8	SF incorporation (63%)
	0.0 ± 0.5	Ternary complex/ Bulk incorporation
Feldspar/Mica*	9.0 ± 0.5	OSS
	7.0 ± 0.5	Weak ISS
	5.7 ± 0.5	Strong ISS
	3.0 ± 0.8	SF incorporation
Quartz (smooth)	5.5 ± 0.5	Strong ISS
	3.0 ± 1.0	SF incorporation
Quartz (rough)	5.7 ± 0.5	Strong ISS
	0.0 ± 0.5	Ternary complex/ Bulk incorporation
Quartz/Feldspar	5.0 ± 0.5	Strong ISS
	3.5 ± 0.5	SF incorporation
Quartz/Mica*	9.0 ± 0.5	OSS
	7.5 ± 0.5	Weak ISS
	6.0 ± 0.5	Strong ISS
	3.0 ± 0.5	SF incorporation
Topaz (smooth)	4.0 ± 0.5	SF incorporation
Topaz (rough)	6.0 ± 0.5	Strong ISS
	2.8 ± 1.6	SF incorporation
Mica (smooth)*	9.0 ± 0.5	OSS
	7.0 ± 0.5	Weak ISS
	6.0 ± 0.5	Strong ISS
	3.0 ± 1.0	SF incorporation
Mica (rough)*	7.5 ± 0.5	Weak ISS
	5.0 ± 0.5	Strong ISS

	3.0 ± 1.0	SF incorporation

*mineral phases containing Fe; where Fe quenching occurs equation (1) is no longer applicable, and the number of coordinating water molecules would be lower than given here

Most lifetime points were measured on feldspar grains, which is why the analysis for feldspar is the most reliable. Feldspar mineral grains with a low surface roughness primarily form strong ISS complexes, but surface incorporation and weak ISS complexes also occur. Surface incorporation seems to become the main retention mechanism, along with strong ISS complexes where surface roughness is high. Weak ISS and OSS also occur, primarily in areas where a high sorption uptake can be observed. At feldspar/mica grain boundaries ISS complexes of varying strength as well as OSS complexes are formed. On pixels, where we observed the high red-shift of the above described ternary complex formation or complete incorporation, long luminescence lifetimes for a secondary species were measured, showing that no more water remains in Cm(III)'s hydration shell.

On quartz mineral grains strong ISS complexes are found on areas with both low and high surface roughness. Surface incorporation took place mainly on smoother quartz surfaces, while ternary complex formation was more likely to occur on rougher quartz surfaces such as surface pits. As with feldspar ternary complexes/incorporated species on quartz show no more water coordinating Cm(III). Along the quartz grain boundaries to feldspar and mica surface incorporation and strong ISS could be seen.

Unfortunately, for mica a detailed lifetime analysis is not useful due to Fe quenching.

Topaz mineral grains with a low surface roughness show SF incorporation of Cm(III), while on areas with a higher surface roughness (surface cracks and mineral boundaries) strong ISS complexes occurred additionally.

3.2 Sorption of Cm(III) on Bukov gneiss

Mineralogy of the Bukov gneiss

Visual inspection of the Bukov gneiss thin section reveals smaller (ten to a few hundred µm) and more diverse mineral grains than for the Eibenstock granite (see Figure 5 a). The PXRD results confirmed this optical assessment, and we identify the minerals as quartz (white), feldspar (grey), amphibole (black) and mica (dark-green), with amphibole and mica being associated with each other.

For an exact determination of the minerals located on the surface, Raman-microscopy was used (see SI Figure S11 for selected spectra) to investigate four different ROIs (see Figure 5 and Figure S7 – S9). Feldspar, amphibole and quartz were found in each area, while phases such as chlorite (ROI 2), titanite (ROI 2), mica (ROI 3), or pyrite (ROI 4) could only be observed in individual areas. Raman-spectra for amphibole, chlorite, and mica are quite similar, but the phases can be distinguished optically. Chlorite was identified by its needle-like structure, while amphibole and mica have different appearances, looking more smooth or rough, respectively. ROI 1 shown in Figure 6 a) consists primarily of amphibole, quartz and feldspar.

Surface topography

Using vertical scanning interferometry, the surface topography of the thin section sample was measured and S_q maps (see Figure 5 b) were generated in order to quantify the surface variations. Figure 6 b shows the surface roughness of ROI 1 (see Figures S7 – S9 for ROIs 2 – 4). The surface roughness parameter S_q determined in ROI 1 is lowest on quartz (69 ± 16 nm), intermediate on feldspar (110 ± 12 nm) and highest on amphibole (141 ± 34 nm), very similar to what we found for Eibenstock granite. As with the Eibenstock granite those are average S_q values resulting from areas exhibiting high surface roughness around pits and cracks and smooth areas between those features.

Amphibole surfaces are characterized by deep surface cracks of up to 1.3 µm. Similar to the Eibenstock sample the feldspar surfaces exhibit surface pits, however at larger depth of up to 590 nm. Singular surface pits located in quartz can reach depths of 1.1 µm, but otherwise the surface is the smoothest.

The grain boundaries are distinctly visible in the roughness maps with height differences of up to 140 nm between feldspar and amphibole leading to S_q values at a maximum of 123 ± 68 nm. The height difference and surface roughness ($\Delta h = 545$ nm; $S_q = 140 \pm 7$ nm) of the quartz/amphibole grain boundary are larger in comparison to the quartz/feldspar grain boundary ($\Delta h = 375$ nm; $S_q = 31 \pm 22$ nm).

Sorption uptake of Eu(III)/Cm(III)

Sorption on bulk powder material of Bukov gneiss was quantified as a function of pH using a $5 \cdot 10^{-7}$ M Eu(III) solution spiked with 70 Bq (135 pmol) of ^{152}Eu. Eu(III) was here used as an analogue for Cm(III). The relative uptake as a function of pH of Eu(III) and Cm(III) is near identical for both trivalent metals on the two rocks as seen in Figure S1. (a) Up to pH 3 no metal uptake from the solution can be observed, while (b) from pH 3 to 5.2 sorption increases to

around 20%. (c) Complete sorption is reached at pH 7.5 (d) with no further changes in sorption uptake occurring at higher pH. As previously described for Eibenstock granite, we then proceed to quantify the sorption uptake and characterize the speciation of Cm(III) spatially-resolved on the individual mineral phases.

Calibrated autoradiography shows highest sorption uptake of Cm(III) on amphibole and mica (see Figure *5* c and Figures S6 – S9) corresponding to 300 – 1100 pmol/cm^2. This is significantly higher than on Eibenstock granite (~ 330 pmol/cm²). At the same time, Cm(III) uptake on feldspar and quartz phases is significantly lower at only 20 – 100 pmol/cm^2. Overall, the sorption on the thin section can be seen as heterogeneous, partially varying on the same mineral phases by one order of magnitude. Sorption uptake hotspots correlate with increased surface roughness, especially on amphibole and mica (see Figure 5 a and b). A slight decrease of signal is observed from the upper right to the lower left, probably due to a minor tilt of the sample on the autoradiography imaging plate, which had no impact on the following measurements.

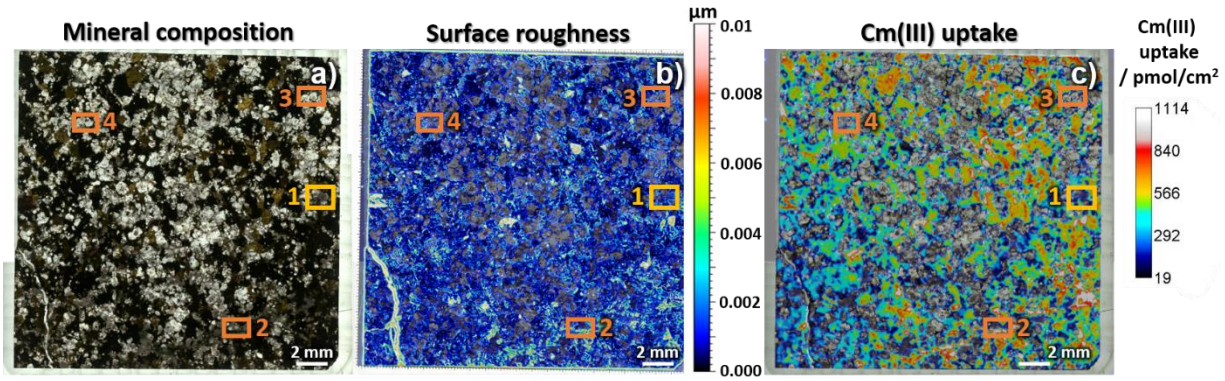

Figure 5: a) Optical image of the Bukov gneiss thin section, b) surface roughness determined using interferometry and c) Cm(III) sorption uptake determined using quantitative autoradiography.

Speciation of Cm(III)

The speciation of Cm(III) was again determined using µTRLFS. Highest Cm(III) LIs were found on feldspar, less on quartz, and almost no signal was detected on amphibole, mica, chlorite, and pyrite. Low signal intensities can again be traced back to Fe quenching, since autoradiography detected high amounts of sorption on mica and amphibole grains. In the following we will discuss the sorption behavior of Cm(III) on ROI 1 in detail (see Figure 6), nevertheless the results of the other ROIs (see Figure S7-S9) will contribute to the discussion.

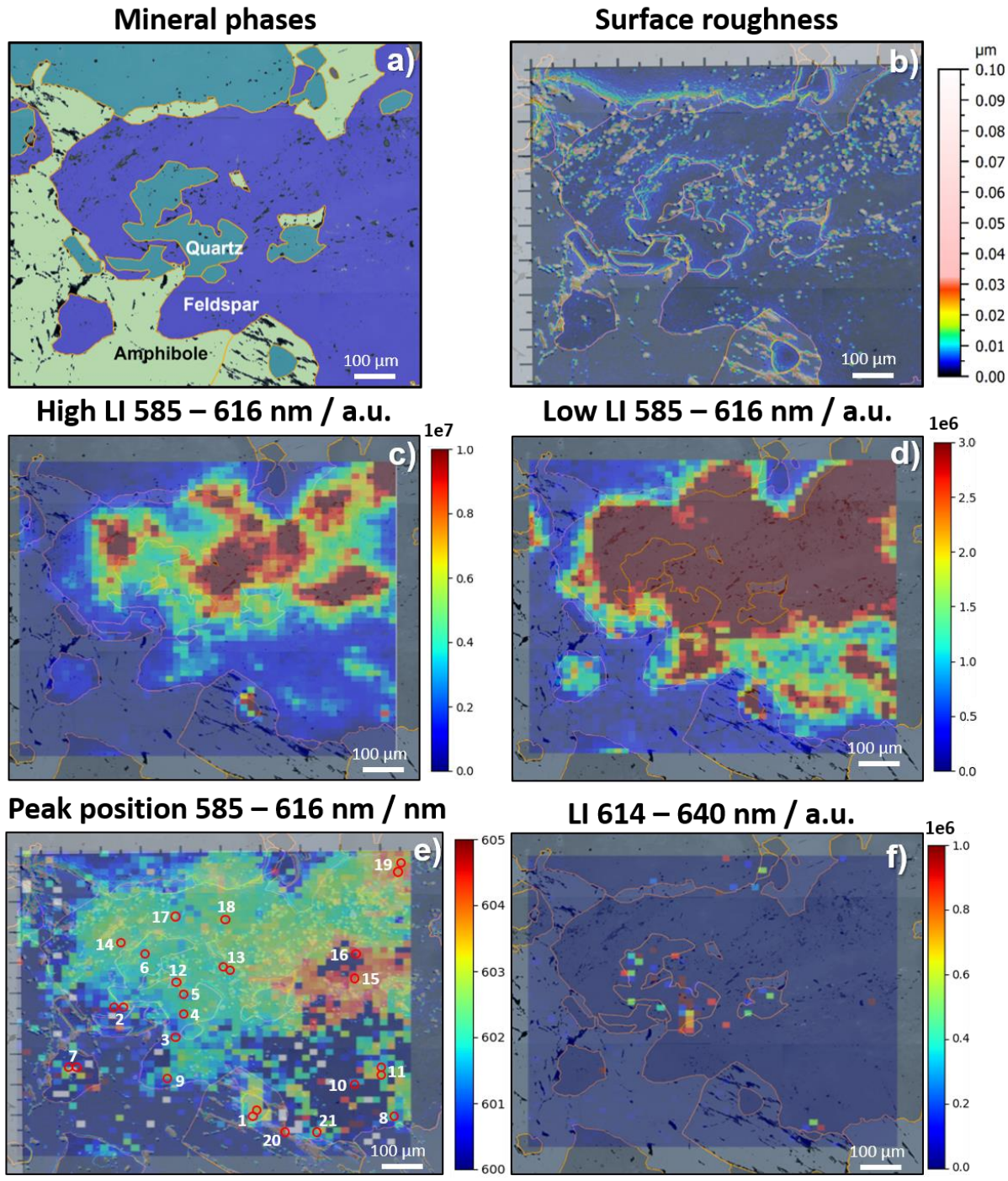

Figure 6: Analysis of ROI 1 on Bukov gneiss: a) mineral composition (Raman-microscopy), b) surface roughness (S_q; interferometry), c) high luminescence regime of Cm(III) (µTRLFS; integral area) and d) low luminescence regime of Cm(III) (µTRLFS; integral area), e) by Gaussian peak fitting obtained peak maxima of the Cm(III) peaks (µTRLFS) and f) luminescence intensity of Cm(III) at higher wavelengths (µTRLFS; integral area).

ROI 1 on Bukov gneiss consists primarily of feldspar, quartz, and amphibole (see Figure 6 a). Areas with a high surface roughness can be seen around feldspar surface pits, amphibole cracks and grain boundaries of quartz with feldspar and mica (see Figure 6 b). The surface pits on feldspar are clustered thus generating areas on feldspar with a high surface roughness, while the remaining surface is relatively smooth.

Similar to our findings for Eibenstock granite, we observe large differences in sorption uptake on quartz and feldspar (see Figure 6 c). On feldspar it is directly obvious that differences in uptake are correlated with the measured surface roughness with rougher areas again showing higher uptake. This is most obvious for the lower right corner of the ROI, which has the lowest surface roughness of the feldspar grain and also by far the lowest sorption uptake. The same also occurs on quartz, but we have reduced the LI scale in order to visualize the areas with increased sorption on quartz (see Figure 6 d). The same map also reveals additional heterogeneity within the area of low uptake on feldspar.

To characterize the speciation of adsorbed Cm(III) the extent of luminescence peak shifting was determined by applying a Gaussian fit to all luminescence spectra (see Figure 6 e).

As on granite Cm(III) luminescence peaks are more red-shifted in feldspar areas with a higher surface roughness. Here, peak maxima around 603 to 605 nm indicate strong inner-sphere complexation.[49] In contrast, on smoother feldspar areas, the maxima are located between 602 and 603 nm pointing toward weaker inner-sphere complexation. [21, 49] However, luminescence intensity was in some areas so low that no fit was possible.

On quartz the peak maxima distribution is narrower with peak maxima ranging from 602 – 603 nm, indicating weak inner-sphere sorption.[50] Further, some luminescence spectra on quartz and in the quartz/feldspar mineral grain boundary exhibit a second Cm(III) peak with a high red-shift of 623 up to 626 nm (see Figure 6 f). As discussed above, the strong peak shift corresponds to either ternary-complex formation or mineral bulk incorporation.

Once again we combine the spectral information with lifetime measurements to obtain a more complete picture of Cm(III)'s speciation on Bukov gneiss. In Table 2 the identified species on each mineral corresponding to the minerals surface roughness or mineral grain boundary on all investigated regions of interest are listed, which are based on a total of 91 lifetimes measurements (see Table S4).

Table 2: Summary of measured lifetimes on all regions of interest on Bukov gneiss corresponding to mineral form and its topography features (ISS = inner-sphere sorption, OSS = outer-sphere sorption, SF = surface). For details the reader is referred to section 3.2. The error 0.5 for calculated water molecules originates from the (1) Kimura equation if only few data points or data points of the exact same value exist. For data sets with multiple data points the error was calculated by the simple standard deviation. Smooth and rough surfaces were determined by visual inspection of the S_q distribution maps.

Mineral form	**n(H_2O)**	**Species**
Feldspar (smooth)	9.0 ± 0.5	OSS (14%)
	7.2 ± 0.4	Weak ISS (24%)
	5.7 ± 0.5	Strong ISS (33%)

	3.5 ± 0.8	SF incorporation (29%)
Feldspar (rough)	7.3 ± 0.5	Weak ISS (23%)
	5.3 ± 0.4	Strong ISS (31%)
	2.5 ± 1.3	SF incorporation (46%)
Feldspar/ Mica*	9.0 ± 0.5	OSS
	7.0 ± 0.5	Weak ISS
Feldspar/Amphibole*	7.7 ± 0.5	Weak ISS
	5.7 ± 0.5	Strong ISS
Quartz (smooth)	7.5 ± 0.5	Weak ISS
	6.0 ± 0.5	Strong ISS
	3.0 ± 0.5	SF incorporation
Quartz (rough)	3.0 ± 1	SF incorporation
	0.0 ± 0.5	Ternary complex/ Bulk incorporation
Quartz/Feldspar	9.0 ± 0.5	OSS (18%)
	7.3 ± 0.4	Weak ISS (24%)
	5.4 ± 0.5	Strong ISS (29%)
	3.0 ± 0.9	SF incorporation (29%)
Quartz/Amphibole*	8.0 ± 0.5	Weak ISS
	6.0 ± 0.5	Strong ISS
Amphibole*	7.7 ± 0.5	Weak ISS
	6.0 ± 0.5	Strong ISS

*mineral phases containing Fe; where Fe quenching occurs equation (1) is no longer applicable, and the number of coordinating water molecules would be lower than given here

Most lifetimes measurements were once more taken on feldspar, making the feldspar data analysis most reliable and detailed. On feldspar with a low surface roughness, ISS complexes of all bond strengths are formed. Mainly strong ISS complexes are formed, followed by surface incorporation, and weak ISS, while OSS could also be observed in a few spots. On feldspar with higher surface roughness generally stronger bound complexes are formed, mainly surface incorporation species, but also strong and weak ISS. The feldspar/mica and feldspar/amphibole mineral grain boundaries show similar sorption behavior, showing weak ISS and OSS, but Fe quenching may impact lifetimes here.

Quartz areas with low surface roughness show mainly weak and strong ISS and surface incorporation. In comparison rougher quartz areas again show a shift towards more strongly bound complexes, primarily ternary complex formation/mineral incorporation and surface incorporation species. On pixels with Cm(III) ternary complexes/mineral incorporation we measured long lifetimes, showing that no water remains in the hydration sphere, as was also observed on the Eibenstock granite.

The quartz/feldspar grain boundaries show ISS complexes of varying strength as well as outer-sphere sorption. Mainly surface incorporation and strong ISS complexes could be observed, but weak ISS or OSS also occur in some spots. Few lifetime spots could be measured along the quartz/amphibole grain boundary, which correspond to intermediate and weak ISS. However, Fe quenching could also be responsible for decreased luminescence lifetimes.

4. Discussion

By using a combination of calibrated autoradiography and µTRLFS a comprehensive insight into the sorption uptake of Cm(III) on crystalline rock and its molecular mechanisms was obtained. The individual Cm(III) surface species on the different mineral phases of the heterogeneous crystalline rocks could be identified. Sorption uptake is highest on mica and amphibole phases, followed by feldspar, topaz, and quartz. From the shift of the luminescence peaks and the analysis of luminescence lifetimes, the type of surface complex and its strength were derived. ISS complexes of varying strength are formed on nearly all mineral phases, while OSS complexes are formed in regions with very high sorption uptake, likely since here the available surface sites for ISS become saturated. The strength of the formed ISS complexes is lowest on mica. On quartz and feldspar ISS complexes of similar strength are formed. The ISS complexes on quartz show a chemical similarity to each other, while ISS complexes on feldspar display more variability. Ternary complex formation or incorporation of Cm(III) can be seen on quartz, feldspar, and their grain boundary with each other.

The use of vertical scanning interferometry allowed us to correlate surface topography with sorption uptake and speciation on the mineral surface. While mineralogy remains the greatest influence on the sorption process, it is evident for both investigated rocks that topography influences the sorption amount and speciation. Rougher structural features may give rise to a locally increased surface area as well as an increase of reactive surface site density and site reactivity due to increased abundance of structural features such as edge/kink sites and surface defects. Following this approach, we could directly confirm that regions exhibiting a higher surface roughness show an overall higher sorption uptake. We also found a shift to stronger bound Cm(III) surface complexes with increasing surface roughness. We can speculate that kink and defect sites, that appear more numerous in high roughness areas, can form more bonds to Cm(III), resulting in more strongly bound Cm(III).

On feldspar, mica, and topaz surfaces the sorption uptake of Cm(III) on the same mineral grains varies greatly depending on the surface roughness. For instance, on the same feldspar mineral grain sorption uptake may be almost one order of magnitude higher in areas with high surface roughness than in smooth areas. These differences in uptake are confirmed by the autoradiography data. Regions with higher surface roughness showed an increase in sorption uptake by one to two orders of magnitude, which was especially interesting for rough quartz regions. Rough quartz surfaces showed almost the same sorption uptake as feldspar or mica mineral grains. The same trend holds true for mineral grain boundaries, which generally

coincide with areas of high surface roughness. Grain boundaries on Eibenstock granite with a higher surface roughness such as quartz/mica seem to increase the amount of sorption uptake more significantly than a lower roughness grain boundary such as quartz/feldspar. On low roughness mica areas, luminescence detection with µTRLFS was not possible at all, presumably due to the combination of reduced uptake on the smooth surface and Fe quenching. But along the mica grain boundary with quartz and around cracks in the mica surface the higher surface roughness increased the sorption uptake sufficiently to make luminescence detection possible. Surface topography is clearly an important factor that needs to be taken into account to describe the sorption behavior of Cm(III). Future studies should focus on determining the impact of surface roughness on radionuclide retention semi-quantitatively. This is particularly relevant for predictive transport modelling of contaminants with respect to the safety of future nuclear waste repositories.

The differences in sorption behavior on Bukov gneiss and Eibenstock granite are similar to what was previously found for the sorption of Eu(III) on the same rocks.[38, 58] On Eibenstock granite most of the sorption takes place on feldspar and mica. On the larger investigated area in this study we also observed high Cm(III) sorption uptakes on topaz with similar speciation characteristics as on feldspar, likely due to sorption occurring on aluminol binding sites.

One particularly interesting species in this context is the ternary surface complex or incorporation species of Cm(III). We observed species with similar characteristics also in our previous studies with Eu(III). As in this study, incorporation seemed unlikely to have occurred in the short reaction time, so the species was identified as “intrinsic Eu(III)”, i.e. Eu(III) incorporated into the minerals upon their formation, thus unrelated to our experiments. In the case of Cm(III) definitely no intrinsic incorporation of the rare, synthetic element is possible, thus the species must have formed during our experiments. The species’ very large red-shift indicates (near) complete replacement of the hydration shell by stronger ligands, which is confirmed by the species’ long luminescence lifetime. Because the reaction time is only seven days and the species only occurs in areas with very high surface roughness, we currently interpret this species as a ternary complex of a surface incorporation species, likely with silicate or carbonate as an additional ligand.

On Bukov gneiss these ternary complexes formed mainly along mineral grain boundaries, while on Eibenstock granite ternary complexes additionally formed on rough feldspar and quartz regions. This might be caused by a concentration effect, since relatively more Cm(III) sorbs on Eibenstock feldspar and quartz than on those minerals on Bukov gneiss, where other mineral

phases are preferred targets for Cm(III) sorption. Sorption on feldspar and quartz is only observed in regions with a high surface roughness on Bukov gneiss, causing up to two orders of magnitude difference in luminescence intensity on the same mineral grains. When no rough feldspar areas were present in a region of interest, Cm(III) sorption occurs almost entirely along feldspar/quartz mineral grain boundaries, since those exhibit high inherent surface roughness. This means when another mineral phase such as amphibole is the dominating sorption partner, sorption on mineral phases with lower sorption preference is governed by surface roughness.

To analyze the entire sorption system of trivalent metal ions on crystalline rocks we compare the Cm(III) results in this study with our previous studies using Eu(III). Findings obtained in the present study compare well with previous Eu(III) studies.[38, 58] However, one major advantage using Cm(III) is its higher luminescence yield allowing µTRLFS experiments at concentrations down to 1 µM thereby avoiding precipitation of metal(hydroxides), which was hampering studies with Eu(III) that had to be conducted at significantly higher concentrations of 50 µM.[58, 62] Further, Cm(III) as a member of the actinides is a radionuclide which will be present in radioactive waste repositories and is also a better analogue to Am(III)/Pu(III) than Eu(III). Nonetheless, we generally found that the speciation of Cm(III) and Eu(III) on both crystalline rocks is similar as was expected, but we were able to distinguish more species on the mineral surface than previously found for Eu(III)[38] by making use of Cm(III)'s higher luminescence sensitivity The necessary higher Eu(III) concentration in previous studies likely lead to more sorption sites becoming saturated, which we avoid at the lower Cm(III) concentration. Therefore, we identified Cm(III) surface incorporation species on feldspar, quartz, and topaz on both crystalline rocks, which was previously only possible for the Bukov gneiss for Eu(III).[58] For lifetime analysis Cm(III) luminescence is also less influenced by naturally occurring incorporated Eu(III), since the emission of the Eu(III) luminescence only barely overlaps with the Cm(III) emission peaks. Further no natural background of Cm(III) exists that would hinder spectral analysis. Eu(III) luminescence peaks also do not exhibit a peak shift due to complexation, but change their peak ratio.[73] Performing the study with Cm(III) instead of Eu(III) therefore allowed us to gain spatially-resolved insight into sorption uptake and speciation at environmentally relevant concentrations.

5. Conclusions

Our results demonstrate that the sorption of radionuclides such as Cm(III) on multi-mineral samples of natural composition can be well described by combining complementary surface investigation techniques. We combined Raman-microscopy, interferometry, autoradiography, and µTRLFS to illuminate which factors control the retention of radionuclides on a topographically and mineralogically heterogeneous surface. The combination of techniques was applied to two different crystalline rock systems yielding similar results, which demonstrates a general validity and can therefore suggests extrapolation to other systems should be possible. The actinide Cm(III) performs better as a luminescent molecular probe in spatially-resolved sorption studies in comparison to its previously used lanthanide analogue Eu(III), because of the absence of natural background luminescence, its lower detection limit and more straightforward spectral analysis. The use of Cm(III) allowed us to show preferential sorption areas and describe the surface speciation in detail. Correlating the molecular information on Cm(III) speciation with topography data from vertical scanning interferometry showed that surface roughness is one of the major parameters influencing the sorption behavior of trivalent actinides, second only to the rock's mineralogy. With both rock samples and on all minerals a clear trend of higher uptake in regions of higher surface roughness was observed. Remarkably, surface roughness also impacts the strength of Cm(III) binding to the surface, i.e. complexes are stronger where roughness is higher, likely due to higher availability of high denticity surface sites.

Our results directly affect the safety assessment of potential nuclear waste disposal sites. Insights from model studies using powdered material and/or single minerals, while crucial for a fundamental understanding, cannot be applied to more natural systems straightforwardly. Other factors come to control retention such as topography, grain boundary effects, or mineral competition. These effects will have to be considered when upscaling to larger experiments or applying reactive transport models. Derivation of corresponding numerical parameters is the next challenge. To ensure highest safety standards such parameters and their variability need to be taken into consideration for reactive transport modeling of radionuclides for the safety assessments of radioactive waste repository sites.

Acknowledgements

We want to thank Anja Schleicher and Uwe Diettmann from the department of Anorganic and Isotope Geochemistry, GFZ, for preparing thin sections samples for us.

This work has been developed in the frame of the iCross project. We gratefully acknowledge funding provided by the German Federal Ministry of Education and Research (BMBF, Grant 02NUK053) and the Helmholtz Association (Grant SO-093). We further acknowledge financial support to S.Schymura by the Helmholtz-Association (Grant PIE-0007) (CROSSING).

6. Literature

[1] M.J. Apted, J. Ahn, Geological repository systems for safe disposal of spent nuclear fuels and radioactive waste, Woodhead Publishing, 2017.
[2] B. Johnson, A. Newman, J. King, Optimizing high-level nuclear waste disposal within a deep geologic repository, Annals of Operations Research, 253 (2017) 733-755.
[3] K.B. Krauskopf, Geology of high-level nuclear waste disposal, Annual Review of Earth and Planetary Sciences, 16 (1988) 173-200.
[4] J.-S. Kim, S.-K. Kwon, M. Sanchez, G.-C. Cho, Geological storage of high level nuclear waste, KSCE Journal of Civil Engineering, 15 (2011) 721-737.
[5] S. Altmann, 'Geo'chemical research: a key building block for nuclear waste disposal safety cases, Journal of Contaminant Hydrology, 102 (2008) 174-179.
[6] M. Apted, J. Ahn, Multiple-barrier geological repository design and operation strategies for safe disposal of radioactive materials, in: Geological Repository Systems for Safe Disposal of Spent Nuclear Fuels and Radioactive Waste, Elsevier, 2010, pp. 3-28.
[7] B. Ma, L. Charlet, A. Fernandez-Martinez, M. Kang, B. Madé, A review of the retention mechanisms of redox-sensitive radionuclides in multi-barrier systems, Applied Geochemistry, 100 (2019) 414-431.
[8] R. Dohrmann, S. Kaufhold, B. Lundqvist, The role of clays for safe storage of nuclear waste, in: Developments in Clay Science, Elsevier, 2013, pp. 677-710.
[9] W. Hummel, J.W. Schneider, Safety of nuclear waste repositories, CHIMIA International Journal for Chemistry, 59 (2005) 909-915.
[10] M.O. Schwartz, Modelling groundwater contamination above the Asse 2 medium-level nuclear waste repository, Germany, Environmental Earth Sciences, 59 (2009) 277-286.
[11] M.O. Schwartz, Modelling groundwater contamination above a nuclear waste repository at Gorleben, Germany, Hydrogeology Journal, 20 (2012) 533-546.
[12] X. Cao, L. Hu, J. Wang, J. Wang, Regional groundwater flow assessment in a prospective high-level radioactive waste repository of China, Water, 9 (2017) 551.
[13] S. Joyce, L. Hartley, D. Applegate, J. Hoek, P. Jackson, Multi-scale groundwater flow modeling during temperate climate conditions for the safety assessment of the proposed high-level nuclear waste repository site at Forsmark, Sweden, Hydrogeology Journal, 22 (2014) 1233-1249.
[14] P. Oy, Safety case for the disposal of spent nuclear fuel at olkiluoto, in: Synthesis, 2012, pp. 460.
[15] J. Wang, High-level radioactive waste disposal in China: update 2010, Journal of Rock Mechanics and Geotechnical Engineering, 2 (2010) 1-11.
[16] N.P. Laverov, S.V. Yudintsev, B.T. Kochkin, V.I. Malkovsky, The Russian strategy of using crystalline rock as a repository for nuclear waste, Elements, 12 (2016) 253-256.
[17] A. Vokal, M. Brezina, H. Kroupova, M. Ligaunova, Development of methods for efficiency assessment of engineered barriers: Radioactive Waste Repository Authority in: Annual Report 2001, Nuclear Research Institute Rez, 2001.

[18] P.E. Mariner, E.R. Stein, E.A. Kalinina, T. Hadgu, C.F. Jove-Colon, E. Basurto, US Sections Prepared for Future NEA Crystalline Club (CRC) Report on Status of R&D in CRC Countries Investigating Deep Geologic Disposal in Crystalline Rock, in: SAND2018-4566R 662612, Sandia National Lab.(SNL-NM), Albuquerque, NM (United States), 2018.
[19] O. Däuper, A. von Bernstorff, Gesetz zur Suche und Auswahl eines Standortes für die Endlagerung radioaktiver Abfälle–zugleich ein Vorschlag für die Agenda der „Kommission Lagerung hoch radioaktiver Abfallstoffe", Zeitschrift für Umweltrecht, (2014) 24-31.
[20] Long-term safety for the final repository for spent nuclear fuel at Forsmark. Main report of the SR-Site project, in: SKB-TR--11-01(V.2), Swedish Nuclear Fuel and Waste Management Co., 2011.
[21] J. Neumann, H. Brinkmann, S. Britz, J. Lützenkirchen, F. Bok, M. Stockmann, V. Brendler, T. Stumpf, M. Schmidt, A comprehensive study of the sorption mechanism and thermodynamics of f-element sorption onto K-feldspar, Journal of Colloid and Interface Science, 591 (2020) 490-499.
[22] T. Stumpf, A. Bauer, F. Coppin, J.I. Kim, Time-Resolved Laser Fluorescence Spectroscopy Study of the Sorption of Cm(III) onto Smectite and Kaolinite, Environmental Science & Technology, 35 (2001) 3691-3694.
[23] T. Stumpf, J. Tits, C. Walther, E. Wieland, T. Fanghänel, Uptake of trivalent actinides (curium (III)) by hardened cement paste: a time-resolved laser fluorescence spectroscopy study, Journal of Colloid and Interface Science, 276 (2004) 118-124.
[24] T. Kupcik, T. Rabung, J. Lützenkirchen, N. Finck, H. Geckeis, T. Fanghänel, Macroscopic and spectroscopic investigations on Eu(III) and Cm(III) sorption onto bayerite (β-Al $(OH)_3$) and corundum (α-Al_2O_3), Journal of Colloid and Interface Science, 461 (2016) 215-224.
[25] T. Stumpf, T. Rabung, R. Klenze, H. Geckeis, J. Kim, Spectroscopic study of Cm(III) sorption onto γ-alumina, Journal of Colloid and Interface Science, 238 (2001) 219-224.
[26] N. Huittinen, T. Rabung, A. Schnurr, M. Hakanen, J. Lehto, H. Geckeis, New insight into Cm(III) interaction with kaolinite – Influence of mineral dissolution, Geochimica et Cosmochimica Acta, 99 (2012) 100-109.
[27] E. Tertre, G. Berger, E. Simoni, S. Castet, E. Giffaut, M. Loubet, H. Catalette, Europium retention onto clay minerals from 25 to 150 C: experimental measurements, spectroscopic features and sorption modelling, Geochimica et Cosmochimica Acta, 70 (2006) 4563-4578.
[28] T. Rabung, M. Pierret, A. Bauer, H. Geckeis, M. Bradbury, B. Baeyens, Sorption of Eu(III)/Cm(III) on Ca-montmorillonite and Na-illite. Part 1: Batch sorption and time-resolved laser fluorescence spectroscopy experiments, Geochimica et Cosmochimica Acta, 69 (2005) 5393-5402.
[29] K. Chung, R. Klenze, K. Park, P. Paviet-Hartmann, J. Kim, A study of the surface sorption process of Cm(III) on silica by time-resolved laser fluorescence spectroscopy (I), Radiochimica Acta, 82 (1998) 215-220.
[30] N. Huittinen, T. Rabung, J. Lützenkirchen, S. Mitchell, B. Bickmore, J. Lehto, H. Geckeis, Sorption of Cm(III) and Gd(III) onto gibbsite, α-$Al(OH)_3$: A batch and TRLFS study, Journal of Colloid and Interface Science, 332 (2009) 158-164.
[31] A. Schnurr, R. Marsac, T. Rabung, J. Lützenkirchen, H. Geckeis, Sorption of Cm(III) and Eu(III) onto clay minerals under saline conditions: Batch adsorption, laser-fluorescence spectroscopy and modeling, Geochimica et Cosmochimica Acta, 151 (2015) 192-202.
[32] A.S. Kar, S. Kumar, B. Tomar, V. Manchanda, Sorption of curium by silica colloids: Effect of humic acid, Journal of Hazardous Materials, 186 (2011) 1961-1965.
[33] S. Virtanen, S. Meriläinen, M. Eibl, T. Rabung, J. Lehto, N. Huittinen, Sorption competition and kinetics of trivalent cations (Eu, Y and Cm) on corundum (α-Al_2O_3): a batch sorption and TRLFS study, Applied Geochemistry, 92 (2018) 71-81.
[34] G.K. Darbha, T. Schäfer, F. Heberling, A. Lüttge, C. Fischer, Retention of latex colloids on calcite as a function of surface roughness and topography, Langmuir, 26 (2010) 4743-4752.

[35] G.K. Darbha, C. Fischer, J. Luetzenkirchen, T. Schäfer, Site-specific retention of colloids at rough rock surfaces, Environmental Science & Technology, 46 (2012) 9378-9387.
[36] G. Krishna Darbha, C. Fischer, A. Michler, J. Luetzenkirchen, T. Schäfer, F. Heberling, D. Schild, Deposition of latex colloids at rough mineral surfaces: An analogue study using nanopatterned surfaces, Langmuir, 28 (2012) 6606-6617.
[37] C. Fischer, I. Kurganskaya, T. Schäfer, A. Lüttge, Variability of crystal surface reactivity: what do we know?, Applied Geochemistry, 43 (2014) 132-157.
[38] K. Molodtsov, S. Schymura, J. Rothe, K. Dardenne, M. Schmidt, Sorption of Eu(III) on Eibenstock granite studied by µTRLFS: A novel spatially-resolved luminescence-spectroscopic technique, Scientific Reports, 9 (2019) 6287.
[39] W.J. Weber, Radiation and thermal ageing of nuclear waste glass, Procedia Materials Science, 7 (2014) 237-246.
[40] J. Veliscek-Carolan, Separation of actinides from spent nuclear fuel: A review, Journal of Hazardous Materials, 318 (2016) 266-281.
[41] R.C. Ewing, Nuclear waste forms for actinides, Proceedings of the National Academy of Sciences, 96 (1999) 3432-3439.
[42] W. Weber, R. Ewing, C. Catlow, T.D. De La Rubia, L. Hobbs, C. Kinoshita, A. Motta, M. Nastasi, E. Salje, E. Vance, Radiation effects in crystalline ceramics for the immobilization of high-level nuclear waste and plutonium, Journal of Materials Research, 13 (1998) 1434-1484.
[43] T. Standish, J. Chen, R. Jacklin, P. Jakupi, S. Ramamurthy, D. Zagidulin, P. Keech, D. Shoesmith, Corrosion of copper-coated steel high level nuclear waste containers under permanent disposal conditions, Electrochimica Acta, 211 (2016) 331-342.
[44] L. Duro, C. Domènech, M. Grivé, G. Roman-Ross, J. Bruno, K. Källström, Assessment of the evolution of the redox conditions in a low and intermediate level nuclear waste repository (SFR1, Sweden), Applied Geochemistry, 49 (2014) 192-205.
[45] B. Grambow, Mobile fission and activation products in nuclear waste disposal, Journal of Contaminant Hydrology, 102 (2008) 180-186.
[46] A. Heller, A. Barkleit, G. Bernhard, Chemical speciation of trivalent actinides and lanthanides in biological fluids: the dominant in vitro binding form of curium (III) and europium (III) in human urine, Chemical Research in Toxicology, 24 (2011) 193-203.
[47] S. Skanthakumar, M.R. Antonio, R.E. Wilson, L. Soderholm, The curium aqua ion, Inorganic Chemistry, 46 (2007) 3485-3491.
[48] H. Moll, T. Stumpf, M. Merroun, A. Rossberg, S. Selenska-Pobell, G. Bernhard, Time-resolved laser fluorescence spectroscopy study on the interaction of curium (III) with Desulfovibrio äspöensis DSM 10631T, Environmental Science & Technology, 38 (2004) 1455-1459.
[49] S. Stumpf, T. Stumpf, C. Walther, D. Bosbach, T. Fanghänel, Sorption of Cm(III) onto different Feldspar surfaces: a TRLFS study, Radiochimica Acta, 94 (2006) 243-248.
[50] S. Stumpf, T. Stumpf, J. Lützenkirchen, C. Walther, T. Fanghänel, Immobilization of trivalent actinides by sorption onto quartz and incorporation into siliceous bulk: Investigations by TRLFS, Journal of Colloid and Interface Science, 318 (2008) 5-14.
[51] M.M. Fernandes, T. Stumpf, B. Baeyens, C. Walther, M. Bradbury, Spectroscopic Identification of Ternary Cm−Carbonate Surface Complexes, Environmental Science & Technology, 44 (2010) 921-927.
[52] J.I. Kim, R. Klenze, H. Wimmer, Fluorescence spectroscopy of curium (III) and application, European Journal of Solid State and Inorganic Chemistry, 28 (1991) 347-356.
[53] T. Fanghänel, J.I. Kim, R. Klenze, Y. Kato, Formation of Cm(III) chloride complexes in $CaCl_2$ solutions, Journal of Alloys and Compounds, 225 (1995) 308-311.
[54] M. Lopez-Fernandez, H. Moll, M.L. Merroun, Reversible pH-dependent curium (III) biosorption by the bentonite yeast isolate Rhodotorula mucilaginosa BII-R8, Journal of Hazardous Materials, 370 (2019) 156-163.

[55] H. Moll, M. Schmidt, S. Sachs, Curium (III) and europium (III) as luminescence probes for plant cell (Brassica napus) interactions with potentially toxic metals, Journal of Hazardous Materials, 412 (2021) 125251.
[56] M.-H. Baik, W.-J. Cho, P.-S. Hahn, Effects of speciation and carbonate on the sorption of Eu (III) onto granite, Environmental Engineering Research, 9 (2004) 160-167.
[57] K. Ishida, T. Kimura, T. Saito, S. Tanaka, Adsorption of Eu(III) on a heterogeneous surface studied by time-resolved laser fluorescence microscopy (TRLFM), Environmental Science & Technology, 43 (2009) 1744-1749.
[58] K. Molodtsov, M. Demnitz, S. Schymura, F. Jankovský, M. Zuna, V. Havlová, M. Schmidt, Molecular-Level Speciation of Eu(III) Adsorbed on a Migmatized Gneiss As Determined Using μTRLFS, Environmental Science & Technology, 55 (2021) 4871-4879.
[59] B. Lafuente, R.T. Downs, H. Yang, N. Stone, The power of databases: the RRUFF project, in: Highlights in Mineralogical Crystallography, Walter de Gruyter GmbH, 2016, pp. 1-29.
[60] Y. Wang, F. Xie, S. Ma, L. Dong, Review of surface profile measurement techniques based on optical interferometry, Optics and Lasers in Engineering, 93 (2017) 164-170.
[61] T. Kimura, R. Nagaishi, Y. Kato, Z. Yoshida, Luminescence study on solvation of americium (III), curium (III) and several lanthanide (III) ions in nonaqueous and binary mixed solvents, Radiochimica Acta, 89 (2001) 125-130.
[62] M.J. Kang, P.S. Hahn, Adsorption behavior of aqueous europium on kaolinite under various disposal conditions, Korean Journal of Chemical Engineering, 21 (2004) 419-424.
[63] X. Tan, M. Fang, J. Li, Y. Lu, X. Wang, Adsorption of Eu(III) onto TiO2: effect of pH, concentration, ionic strength and soil fulvic acid, Journal of Hazardous Materials, 168 (2009) 458-465.
[64] S.M. Britz, Europium sorption experiments with muscovite, orthoclase, and quartz: Modeling of surface complexation and reactive transport, Dissertation, Fakultät Architektur, Bauingenieurwesen und Umweltwissenschaften, Technische Universität Carolo-Wilhelmina zu Braunschweig, 2018.
[65] C. Richter, Sorption of environmentally relevant radionuclides (U(VI), Np(V)) and lanthanides (Nd(III)) on feldspar and mica, Dissertation, School of Science, TU Dresden, Dresden, 2015.
[66] J. Tits, T. Stumpf, T. Rabung, E. Wieland, T. Fanghänel, Uptake of Cm(III) and Eu(III) by calcium silicate hydrates: a solution chemistry and time-resolved laser fluorescence spectroscopy study, Environmental Science & Technology, 37 (2003) 3568-3573.
[67] J.-M. Wolter, K. Schmeide, N. Huittinen, T. Stumpf, Cm(III) retention by calcium silicate hydrate (CSH) gel and secondary alteration phases in carbonate solutions with high ionic strength: A site-selective TRLFS study, Scientific Reports, 9 (2019) 14255.
[68] T. Rabung, M. Altmaier, V. Neck, T. Fanghänel, A TRLFS study of Cm(III) hydroxide complexes in alkaline $CaCl_2$ solutions, Radiochimica Acta, 96 (2008) 551-560.
[69] M.d.S.M. Fernandes, Spektroskopische Untersuchungen (TRLFS und XAFS) zur Wechselwirkung von dreiwertigen Lanthaniden und Actiniden mit der Mineralphase Calcit, Dissertation, Natural Sciences, Mathematics, and Computer Sciences, Ruprecht-Karls-Universität, Heidelberg, 2006.
[70] N. Huittinen, A.C. Scheinost, Y. Ji, P.M. Kowalski, Y. Arinicheva, A. Wilden, S. Neumeier, T. Stumpf, A spectroscopic and computational study of Cm^{3+} incorporation in lanthanide phosphate rhabdophane ($LnPO_4 \cdot 0.67\ H_2O$) and monazite ($LnPO_4$), Inorganic Chemistry, 57 (2018) 6252-6265.
[71] S.E. Hellebrandt, S. Hofmann, N. Jordan, A. Barkleit, M. Schmidt, Incorporation of Eu(III) into calcite under recrystallization conditions, Scientific Reports, 6 (2016) 33137.
[72] S. Hellebrandt, Grenzflächenreaktionen von Actiniden an Muskovit, Dissertation, School of Science, Technische Universität Dresden, Dresden, 2017.

977 [73] K. Binnemans, Interpretation of europium(III) spectra, Coordination Chemistry Reviews,
978 295 (2015) 1-45.

979

980

981